An efficient approach for inverting rock exhumation from thermochronologic age-elevation relationship

Yuntao Tian[1,2]*, Lili Pan[1], Guihong Zhang[1], Xinbo Yao[1]

[1] Guangdong Provincial Key Laboratory of Geodynamics and Geohazards, School of Earth Sciences and Engineering, Sun Yat-sen University, Guangzhou 510275, China

[2] Southern Marine Science and Engineering Guangdong Laboratory (Zhuhai), Zhuhai 519082, China

*Corresponding author:

Yuntao Tian

tianyuntao@mail.sysu.edu.cn

Abstract

This study implements the least-squares inversion method for solving the exhumation history from thermochornologic age-elevation relationship (AER) based on the linear equation among exhumation rate, age and total exhumation from the closure depth to the Earth surface. Modelling experiments suggest significant and systematic influence of initial geothermal model, the *a priori* exhumation rate and the time interval length on the *a posterior* exhumation history. Lessons learned from the experiments include that (i) the modern geothermal gradient can be used for constraining the initial geothermal model, (ii) a relatively higher *a priori* exhumation rate would lead to systematically lower *a posteriori* exhumation, and *vice versa*, (iii) the variance of the *a priori* exhumation rate controls the variation of the inverted exhumation history, (iv) the choice of time interval length should be optimized for resolving the potential temporal changes in exhumation. Putting together these findings, we implemented a new stepwise inverse modeling method for optimizing the model parameters by comparing the observed and predicted thermochronologic data and modern geothermal gradient to mitigate the model dependencies on the initial parameters. Finally, method demonstration was performed using four synthetic datasets and three natural examples of different exhumation rates and histories. It is shown that the inverted rock exhumation histories from the synthetic datasets match the whole picture of the "truth", although the temporal changes in the magnitude exhumation are underestimated. Modelling of the datasets from natural samples produce geologically reasonable exhumation histories. The code and data used in this work is available in GitHub (https://github.com/yuntao-github/A2E_app).

Key words: Thermochronology; Exhumation; Numerical inversion; Age-elevation relationship; Least-squares method; Geothermal model

1. Introduction

Quantifying rock exhumation from the Earth interior to the surface is important information for better understanding many geological problems, ranging from orogenic growth (e.g., Zeitler et al., 2001; Whipp Jr. et al., 2007) and decay (e.g., House et al., 2001; Hu et al., 2006), to resource and hydrocarbon evaluation and exploration (e.g., Armstrong, 2005; Mcinnes et al., 2005), as well as the underpinning endogenic and exogenic processes and their interactions (e.g., Burbank et al., 2003; Fox et al., 2015; Tian et al., 2015). Various experimental and modeling methods have been invented for estimating the rock exhumation at different crustal levels (e.g., Braun, 2003; Reiners and Brandon, 2006; Anderson et al., 2008; Braun et al., 2012; Fox et al., 2014).

One type of the methods for estimating the rock exhumation in the middle and upper crust relies on thermochronologic cooling ages acquired from by noble gas and fission-track dating of a series of accessory minerals, such as Ar-Ar, fission-track and (U-Th)/He analyses (Ault et al., 2019 and references therein). Based on the closure temperature theory (Dodson, 1973), assuming monotonic cooling, a thermochronologic age records the time duration that a rock cooled through the corresponding closure temperature, which is a function of the kinematics describing fission-track annealing and noble gas diffusion, and rock cooling rate (Dodson, 1973). If the depth of the closure temperature isotherm can be estimated from the crustal temperature field, a time-averaged exhumation rate can be obtained from the cooling age.

Based on the thermochronologic methods and thermo-exhumation modelling, many analytical and numerical tools have been implemented for inverting the exhumation and/or the associated cooling history from thermochronologic data. These tools have different functions, such as inverting temperature history (Laslett et al., 1987; Ketcham, 2005; Gallagher, 2012), determining time-averaged exhumation rates (Brandon et al., 1998; Ehlers, 2005; Willett and

83   Brandon, 2013; Glotzbach et al., 2015; Van Der Beek and Schildgen, 2023), spatiotemporal

84   changes in exhumation (Sutherland et al., 2009; Herman et al., 2013; Fox et al., 2014; Willett et

85   al., 2020), and evolution of exhumation in two or three dimensions given a tectonic framework

86   (Batt and Brandon, 2002; Braun, 2003; Van Der Beek et al., 2010; Valla et al., 2011; Braun et al.,

87   2012).

88   Convincing estimate of exhumation history for a region requires both a proper sampling

89   strategy for thermochronologic data and a robust modeling approach for exhumation inversion,

90   especially when the rock exhumation and its spatiotemporal changes are tectonically controlled

91   (Ehlers and Farley, 2003; Schildgen et al., 2018). A routine and efficient sampling strategy

92   acquires themochronologic ages from an elevation transect over a significant relief and a relatively

93   confined spatial distance. Plotting the age versus elevation, i.e., the age-elevation relationship

94   (AER), and analyzing the slope changes of the plot can provide first-order understanding of the

95   exhumation history (Fitzgerald et al., 1986). Because both the subsurface geothermal field and

96   closure temperature of thermochronometers are functions of the thermal advection and cooling

97   during rock exhumation (e.g., Dodson, 1973; Brandon et al., 1998), as well as the long-wavelength

98   topography (Braun, 2002; Ehlers and Farley, 2003; Glotzbach et al., 2015), Estimating reliable

99   exhumation rates requires to account for temporal variations of the thermal field caused by changes

100 in the thermal and kinematic boundary conditions.

101   Fox et al. (2014) reported a linear inversion modeling method that solves exhumation

102 history from AER, given a combination of *a priori* exhumation rates and assumed geothermal

103 parameters. However, as shown in that study, the inverted exhumation history depends highly on

104 these *a priori* values and geothermal assumptions. Building on that study, we here provide a

109   detailed test on the method and report an improved modeling method that makes use of both the

110   AER and the modern geothermal gradient for inverting exhumation history.

111

112   **2. Linear inversion method**

113   Our inversion of exhumation from thermochronologic data followed the linear inversion

114   approach of Fox et al. (2014). Rock Exhumation from the closure depth of a thermochronometer,

115   z_c, to the Earth's surface can be described as an integral of the exhumation ($\dot{e}$) from the cooling

116   age (τ) to the present (Brandon et al., 1998; Fox et al., 2014). For a set of correlated bedrock

117   samples with a shared history of exhumation rates ($\dot{\mathbf{e}}$), their thermochronologic ages ($\mathbf{A}$) and the

118   corresponding closure depths ($\mathbf{z_c}$) can be expressed by the following equation.

$$119 \qquad \int_{\mathbf{0}}^{\boldsymbol{\tau}} e\, dt = z_c \quad \Rightarrow \quad \mathbf{Ae} = \mathbf{z_c}\, , \qquad (1)$$

120   where $\mathbf{A}$ is a model matrix, with n rows (the total number of samples) and m columns (the total

121   number of time intervals). Each row of the matrix is a discretization of a sample age, which is

122   composed of a number of time lengths (Δt) followed by an age residual (R_i) and a number of zeros.

123   The $\dot{\mathbf{e}}$ is a m-length vector of exhumation rates, and the $\mathbf{z_c}$ is n-length vector of closure depths.

124   This linear equation can be solved using the Least-Squares Regression approach assuming

125   the Gaussian uncertainties and *a priori* mean exhumation rate ($\dot{\boldsymbol{e}}_{pr}$) and associated variance (σ_{pr})

126   (Tarantola, 2005; Fox et al., 2014). Such an approach requires a m*m-sized parameter covariance

127   matrix, $\mathbf{C}$, and a n*n-sized data covariance matrix, $\mathbf{C_\varepsilon}$, which includes the uncertainties on the

128   closure depths. These two matrices can be constructed as equations 2 and 3, respectively.

$$129 \qquad C_{ij} = \begin{cases} \sigma_{pr}^2, & if\ i = j \\ 0, & if\ i \neq j \end{cases} \qquad (2)$$

$$130 \qquad (C_\epsilon)_{ij} = \begin{cases} e_{pr}\epsilon_i\, , & if\ i = j \\ 0, & if\ i \neq j \end{cases}, \qquad (3)$$

134 where $\dot{e}_{pr}$ and σ_{pr} are the *a priori* exhumation and the associated variance, and the ε_i is analytical

135 uncertainty of the age data. The construction of the data covariance matrix assumes the age data

136 are uncorrelated. Worth noting is that previous studies used different constructions of the data

137 covariance, changing from using the analytical age uncertainties (Fox et al., 2014; Fox et al., 2015)

138 to constant values (Jiao et al., 2017; Stalder et al., 2020).

139   Given the above model parameters, the equation 1 has a maximum likelihood solution for

140 the exhumation rate vector:

141
$$\mathbf{e}_{po} = \mathbf{e}_{pr} + \mathbf{CA}^T(\mathbf{ACA}^T + \mathbf{C_\epsilon})^{-1}(\mathbf{z}_c - \mathbf{Ae}_{pr}), \tag{4}$$

142 where $\dot{\mathbf{e}}_{pr}$ is a n-length vector of $\dot{e}_{pr}$, $\mathbf{z}_c$ is the n-length vector of closure depths calculated using a

143 combination of exhumation and geothermal model parameters (see section 3). The $\dot{\mathbf{e}}_{po}$ is the

144 posteriori maximum likelihood estimate of the exhumation rate, with a covariance matrix, $\mathbf{C}_{po}$,

145 which provides an estimate of the uncertainties on the model parameters (equation 5).

146
$$\mathbf{C}_{po} = \mathbf{C} - \mathbf{CA}^T(\mathbf{ACA}^T + \mathbf{C_\epsilon})^{-1}\mathbf{AC} \tag{5}$$

147   The method also provides a model resolution matrix, $\mathbf{R}$, which gives a measure on how

148 well the model estimates correspond to the true values:

149
$$\mathbf{R} = \mathbf{CA}^T(\mathbf{ACA}^T + \mathbf{C_\epsilon})^{-1}\mathrm{A}. \tag{6}$$

150

151 **3. Closure depth and topographic correction**

152   Inversion of the exhumation using the equation 1 requires accurate estimates of the closure

153 depths of the thermochronologic ages ($\mathbf{z}_c$), i.e., the depth of the closure temperatures (Fig. 1). The

154 latter can be determined by modelling the temperature of the crust using a 1D thermal-kinematic

155 model, which accounts for heat conduction, advection and production (Turcotte and Schubert,

156 2002):

161
$$\frac{\partial T_m}{\partial t} = \kappa \frac{\partial^2 T_m}{\partial z^2} + e \frac{\partial T_m}{\partial z} + A_b, \tag{7}$$

162 where A_b is the heat production (in °C/Myr). This function can be numerically solved using a

163 Crank–Nicolson time integration with a set of initial and boundary conditions, such as an initial

164 geothermal gradient (G0) at the start time of the model and surface temperature (Ts) (Turcotte and

165 Schubert, 2002; Fox et al., 2014).

166 The closure temperature (T_c) of a thermochronometer is a function of cooling rate ($\dot{T}$) at

167 the closure time and kinetic parameters of Helium and Argon diffusion and fission-track annealing

168 in mineral phases (Dodson, 1973):

169
$$T = \frac{\Omega R T_c^2}{E_a} \exp\left(\frac{-E_a}{R T_c}\right), \tag{8}$$

170 where Ω and E_a are the diffusion frequency factor normalized by the mineral size and geometry,

171 and activation energy, respectively. Parameter R is the gas law constant. See reviews by Reiners

172 and Brandon (2006) for the Ω and E_a parameter values for different thermochronometers.

173 The cooling rate ($\dot{T}$) can be computed from the derivative of transient geotherms, $T_m(t,z)$

174 that can be computed using equation 7 (Fox et al., 2014):

175
$$T = \frac{\partial T_m}{\partial t} + e \frac{\partial T_m}{\partial z}, \tag{9}$$

176 where $\dot{e}$ is unknown exhumation that can be computed through the equation 1.

177 Combining the equations 7-9, the closure depth of a thermochronological system ($z_{c,m}$) can

178 be numerically computed. This depth also needs a topographic correction, because of the

179 topographic perturbation, p, on the isotherms (Braun, 2002; Ehlers and Farley, 2003; Fox et al.,

180 2014; Glotzbach et al., 2015). Such a perturbation can be determined by the following equation

181 (Mancktelow and Grasemann, 1997; Fox et al., 2014):

182
$$p(\lambda) = \left(\frac{\gamma_0 - \gamma_a}{\gamma_{z_m}}\right) \exp\left(-z_m\left(\frac{e}{2\kappa} + \sqrt{\left(\frac{e}{2\kappa}\right)^2 + (2\pi\kappa)^2}\right) h(\lambda), \tag{10}$$

183   where γ_a is the atmospheric lapse rate, γ_0 and γ_{z_m} are the thermal gradients at the model surface and

184   at the depth z_m. The $h(\lambda)$ is a cosine function expression of the model surface topography, which

185   can be determined using the discrete Fast Fourier Transform at the frequency domain. Here we use

186   the SRTM30 data for computing the topography of regions of interests.

187   Finally, the closure depth of the z_c is corrected by the topographic perturbation (e.g.,

188   Brandon et al., 1998):

189
$$(z_c)_i = (z_{c,m})_i - p_i + h_i, \tag{11}$$

190   where $z_{c,m}$ is the closure depth calculated using the 1D geothermal model, p and h are the

191   topographic perturbation and elevation difference with respect to the mean elevation at the sample

192   site (Fig. 1), and the i denotes the i-th age.

193   As shown by the equations 7, 8 and 9, the closure depth is a non-linear function of rock

194   cooling and exhumation. Therefore, the problem of interest is non-linear, which can be addressed

195   by iterative numerical modelling methods. In this work, the solution of exhumation is

196   approximated by coupling and iterating the linear inversion and closure depth modeling. As shown

197   in Tarantola (2005) and Fox et al. (2014), the algorithm converges in a few iterations and produces

198   stable outputs.

199

200 **4. Model evaluation**

201   Quantitative model assessment relies on a misfit value, i.e., the difference between

202   observed and predicted ages weighted by the observed analytical uncertainty:

203
$$\Phi_\tau = \sqrt{\frac{1}{N}\sum_{i=1}^{N}\left(\frac{\tau_{prd,i}-\tau_{obs,i}}{\varepsilon_i}\right)^2}, \tag{12}$$

204   where $\tau_{obs,i}$ and $\tau_{prd,i}$ are the observed and predicted i-th age calculated from the exhumation history,

205   and ε_i is the uncertainty of the observed i-th age. Following Fox et al. (2014), both the *a priori* and

209 *a posteriori* misfits, $\Phi_{\tau, pr}$ and $\Phi_{\tau, po}$, are determined for the models. The difference between these

210 two misfit values provides a measure of the model improvements. A smaller posteriori misfit value

211 indicates an improved model result, and *vice versa*.

Deleted: data fitness

212   To evaluate the geothermal parameters, we also determined the misfit value of the

213 predicted to the observed modern geothermal gradient value using the following equation:

214
$$\Phi_\gamma = \sqrt{\left(\frac{\gamma_{prd}-\gamma_{obs}}{\varepsilon_\gamma}\right)^2},\qquad(13)$$

215 where γ_{prd} and γ_{obs} are the predicted and observed geothermal gradients, and ε_γ is the uncertainty

216 of the observed value. Because the depth-temperature curves are slightly non-linear, the predicted

217 geothermal gradient (γ_{prd}) is calculated as a mean value for the upper 1 km of the model. Similar

218 as the assessment of age data, we also determined the *a priori* and *a posteriori* misfits, $\Phi_{\gamma, pr}$ and

219 $\Phi_{\gamma, po}$ values for assessing the geothermal parameters.

220

221 **5. The reference inverse model**

222   Following Willett and Brandon (2013) and Fox et al. (2014), here we use the published

223 AFT data acquired from Denali Massif (Fitzgerald et al., 1995) for method demonstration (Fig.

224 2a). A break-in-slope is shown by the AER at ~7-6 Ma, indicating a coeval change in slope, i.e.,

Deleted: change

225 the apparent exhumation rate (Fitzgerald et al., 1995), increasing from 0.17 ± 0.04 km/Myr to 1.2

226 $\pm$ 0.6 km/Myr (Fig. 2b). AER regression of young dates from the lower part of the transect

227 (between 4.3-2.0 km) also predicts a closure depth that is the intercept at -3.3 ± 3.4 km (Fig. 2b).

228 However, using the present geothermal gradient (38.9 °C/km) (Fox et al., 2014) and a nominal

229 closure temperature of AFT method (110 °C) (Reiners and Brandon, 2006) and a -12 °C surface

230 temperature (Fox et al., 2014), the closure depth is predicted as ~3.1 km beneath the mean elevation

233 (~4 km), which is equivalent to an elevation of ~0.9 km. This closure depth is significantly higher

234 than the intercept (-3.3 ± 3.4 km). Such a difference indicates the AER slope of the lower part

235 overestimates the exhumation rates since ~7-6 Ma.

236   Following the protocol outlined in Fox et al. (2014), the reference inverse model uses the

237 following parameters, a start time at 25 Ma, a time interval (Δt) of 2.5 Myr, a 4020 m mean

238 elevation, a -12 °C surface temperature, *a priori* exhumation rate of 0.5 ± 0.15 km/Myr, a 24 °C/km

239 initial geothermal gradient, a 38.9 °C/km present geothermal gradient, a model block with a

240 thickness of 80 km, and a 30 km^2/Myr thermal diffusivity.

241   The exhumation history output of the reference model is shown in Fig. 3. The inversion

242 results reveal an more than two-fold increase of exhumation rate to a value of ~0.6 km/Myr at 7.5

243 Ma (Fig. 3b), consistent with the development of the break-in-slope in the AER. The model also

244 shows a gradual decrease of exhumation rate from *a priori* exhumation rate (0.5 km/Myr) to 0.3

245 km/Myr from 25 Ma to 7.5 Ma. The invariant exhumation during the starting stage resulted from

246 the fact that all ages are younger than 17.5 Ma, and thus the data have no resolution for the time

247 span. These results are similar to those of Fox et al. (2014). The posteriori misfit for the age is

248 1.88, significantly smaller than that of the priori model (4.51), suggesting the improvement by the

249 inverse modeling (Fig. 3b). Such a model also provides reasonable fit to the modern temperature

250 field, as shown by the small misfit (0.39) in the geothermal gradient (Fig. 3b).

251   The resolution of the inverted exhumation history can be assessed by the resolution matrix

252 **R** (equation 6). Imaging of the matrix shows the model provides no resolution for the time period

253 before 17.5 Ma (Fig. 3c), consistent with the fact that the oldest input age is younger than 16.1 ±

254 0.9 Ma. For the time span between 15 and 5 Ma, the model resolution is high, as shown by the

255 diagonal elements of the matrix, with the highest resolution at 7.5-5 Ma span, including eight age

268   date points (Fig. 3c). The most recent two phases of exhumation (5-0 Ma) are less resolved, as

269   shown by the nearly equal resolution values for the two phases, i.e., the latest four pixels of the

270   matrix (Fig. 3c). This is because no input ages fall into this time span, when the modeled

271   exhumation results are time-averaged values. The slight decrease in the last stage reflects changes

272   in geothermal gradient.

273   For assessing the correlation among model parameters, the calculated covariance matrix is

274   scaled by the diagonal covariance matrix (Fox et al., 2014):

275
$$C_{\xi\beta} = \frac{C_{\xi\beta}}{\sqrt{C_{\xi\xi}}\sqrt{C_{\beta\beta}}} . \tag{14}$$

276   The correlation matrix for the reference model is shown in Fig. 3d. The diagonal correlation

277   values are 1 and off-diagonal ones are dominantly negative, indicating anti-correlated uncertainties

278   (Fig. 3d), which suggests exhumation parameters were not resolved independently by the modeling.

279   In fact, it is expected to have the anti-correlation, because, given two steps of rock exhumation,

280   decreasing the exhumation during one step would increase that of the other step.

281

282   **6. Dependence on model parameters and proposed solutions**

283   Here we use the Denali data set for demonstrating the influences of (1) the initial

284   geothermal parameters, (2 and 3) the *a priori* mean and variance values of the exhumation rates,

285   and (4) time interval length on the inverted exhumation history. Also discussed in this section are

286   the solutions for optimizing the model setup for these parameters.

287

288   **6.1. Dependence on initial thermal model**

289   Different initial model geothermal parameters would lead isotherms to shift either

290   downward to greater depths or upwards to the Earth surface, and either compression or expansion

295   among isotherms. Therefore, the initial thermal models have systematic influence on the closure

296   depths and consequently the *a posterior* exhumation.

297   This is demonstrated by modelling experiments presented in Figure 4. Using a relatively

298   lower initial geothermal gradient produces relatively higher *a posterior* exhumation rates

299   (comparing the models shown in Figs. 4a-4f), and *vice versa*. Such an influence is significant even

300   for the time and elevation intervals with multiple age constraints (10-5.0 Ma). For example, using

301   relatively lower geothermal gradients of <22 °C/km would yield significantly higher average

302   exhumation rates of >0.75 km/Myr for the last two stages (<5 Ma) (Figs. 4a-4c) than those (<0.6

303   km/Myr) using higher initial geothermal gradients of ≥26 °C/km (Figs. 4d-f). Further, it is also

304   shown that models using higher and lower prior geothermal gradients of <20 °C/km (Figs. 4a-4b)

305   and >30 °C/km (Figs. 4e-4f) yield worse misfits ($\Phi_{\gamma,\ po}$ > 1) for the observed present-day

306   geothermal gradient than those ($\Phi_{\gamma,\ po}$ < 1) using medium initial gradients (22-26 °C/km) (Figs. 3

307   and 4c-4d).

308   These results highlight the importance of taking geothermal parameters into account in

309   inverting the exhumation history and model evaluation. We proposed to run a set of models using

310   different *a priori* geothermal parameters, especially the initial geothermal gradient, to search for

311   the proper intitial geothermal setup that provides reasonable fits to both the ages and the modern

312   geothermal gradient (see section 7 for details).

313

314   **6.2. Dependence on the *a priori* exhumation rate**

315   Both the mean and variance of the *a priori* exhumation rate have important influences on

316   the model solution for the maximum likelihood estimation method. Our modeling experiments

317   show that the mean value of the *a priori* exhumation has systematic influences on the inverted

326   exhumation. Similar to the reference model, exhumation of the preceding three stages (25-17.5

327   Ma) without age constraints is the same as the *a priori* input. For the following stages, a relatively

328   higher mean value of the *a priori* exhumation results in relatively lower *a posterior*i exhumation

329   rates (comparing different models presented in Fig. 5). For example, models using the mean *a*

330   *priori* exhumation of ≤0.4 km/Myr yield *a posterior* exhumation of 0.5-0.9 km/Myr for the stages

331   <7.5 Ma (Figs. 5a-5c), whereas those using a higher *a priori* value (≥ 0.6 km/Myr) result in *a*

332   *posterior* exhumation of 0.45-0.6 km/Myr for the same stages (Figs. 5d-5f). This is because a

333   relatively higher *a priori* value, which would be used for calculating thermal models, would lead

334   to a quicker increase in geothermal gradient and thus relatively shallower closure depths and

335   relatively lower exhumation rates.

336   The variance of the *a priori* exhumation rate has important influence on both the

337   exhumation rates and the posterior variance. Models with lower *a priori* variances yield less

338   variations in the *a posterior* exhumation history, and *vice versa* (comparing models in Fig. 6).

339   Further, models using the input variance of the *a priori* exhumation of 0.2-0.3 km/Myr (40-60%

340   of the mean value), the variation of the inverted exhumation history becomes stable (Figs. 3, 6c-

341   6d). Given that the uncertainty of the input age data, which is often 10%-20% at a two-sigma level,

342   larger variance of the inverted exhumation would be unreasonable (Figs. 6e-6f), especially when

343   multiple age data are available at different elevations.

344   We proposed to run a set of models using different *a priori* mean value of erosion rates to

345   search for the one that provides appropriate fits to both the ages and the modern geothermal

346   gradient. As to the *a priori* variance, we propose to use a value 30-70% of the *a priori* erosion rate.

347   Future applications of the method may need to test a set of the variance inputs so as to get a stable

355 exhumation output. Larger *a priori* variance would lead to larger uncertainties for the exhumation

356 rates, which is unreasonable and non-meaning for geological studies.

357

6.3. Dependence on time interval length

359   Constraining the onset time of major changes in exhumation rates is one of the important

360 tasks for inverting the exhumation history from thermochronologic data. Using a large time

361 interval length cannot accurately capture the potential transition time of exhumation rates. As

362 shown in the Figs. 7b-7d, models using time lengths of ≤3.5 Ma show an abrupt increase in

363 exhumation at 7-6 Ma, consistent with that shown in AER plot. However, the models using a large

364 time interval length (≥4.5 Ma) overestimate the onset time of the enhanced exhumation (Figs. 7e-

365 7f). Further, a relatively shorter time length would smooth temporal changes in exhumation rates,

366 leading to an underestimating of the variations. For example, as shown in the Fig. 7a, the model

367 using a relatively shorter time length (0.5 Ma) yields an exhumation variation between 0.35-0.60

368 km/Myr, significantly lower than those using relatively larger time interval lengths (Figs. 7b-7f).

369 In addition, a shorter time length also significantly increases the computational time and resources,

370 especially when processing a large number of vertical transects.

371   Given the interests in major exhumation changes, we propose the time interval length (Δt)

372 should be optimized for constraining the transitional time and the associated exhumation changes.

373 Therefore, the time interval length should be set as the absolute uncertainty at two sigma levels at

374 the break point (τ_b) (equation 15). If the break point is unclear in AER, we suggest to use the

375 absolute uncertainty at two-three sigma levels at the median age value (τ) (equation 15), so as to

376 focus on the time intervals where ages cluster.

$$\Delta\tau = \begin{cases} \delta\tau_b, & if\ a\ break\ in\ slope\ exists \\ \delta\tau, & if\ no\ clear\ break\ in\ AER \end{cases} , \qquad (15)$$

379   where δ is the relative age uncertainty at two sigma levels, varying between 10%-20% among

380   different studies. Following this method, the Denali case should use a time length of ~1.5 Ma (7

381   Ma × 20%), slightly lower than that used in the reference model (Fig. 3).

382

383   **7. A new modeling guideline**

384   Following the modelling protocol outlined above, a stepwise modeling guideline is

385   developed for addressing the model dependencies on the initial geothermal parameter, the *a priori*

386   exhumation rates and time interval length. As illustrated in the Figure 8, the approach includes the

387   following three steps.

388   (i) Estimating a time-averaged erosion rate. Dividing each nominal closure depth, which

389   can be estimated from the nominal closure temperatures and the modern geothermal gradient, by

390   the corresponding age results in a time-averaged erosion rate. Then, a mean value can be

391   determined by averaging the rates. Such a mean value and assumed variance (30% - 50% in this

392   work) will be used as the *a priori* erosion rate.

393   (ii) Optimizing the fit to the modern geothermal gradient. This step runs a set of inversion

394   models (20 in this work) using different geothermal gradients, ranging from 50% to 120% of the

395   modern value, together with the *a priori* erosion rate estimated in the first step, for determining

396   the initial geothermal gradient that yields the maximum fit to the modern value, i.e., the minimum

397   Φ_γ (equation 13).

398   (iii) Optimizing the fit to both the age data and the geothermal gradient. Given the model

399   dependence on the geothermal parameters (see section 6.1), a comprehensive evaluation of the

400   models should assess not only the age misfit (Φ_τ), but also that of the geothermal gradient (Φ_γ). In

401   the third step, a set of inversion models (20 in this work) are run using different *a priori* erosion

Deleted: strategy

Deleted: Putting together the lessons learned from the above modelling experiments

Deleted: new

Deleted: strategy

Deleted: develops

Deleted: 60

409 rates, changing from 10% to 200% of the mean value estimated in the first step, together with the

410 estimated geothermal gradient by the second step, to search for the model that provides the best fit

411 to both the age data and the modern geothermal gradient. This study uses the following compound

412 misfit function to evaluate the models:

413
$$\Phi = \Phi_\tau + \Phi_\gamma / \sqrt{N}, \qquad (17)$$

414 where Φ_τ and Φ_γ are misfit values for the age and geothermal gradient calculated using the

415 equations 12 and 13, and N is the number of age inputs. Dividing Φ_γ by the square root of N in this

416 equation, as also done for calculating the Φ_τ (equation 12), means that the modern geothermal

417 gradient is given the same weight as an age input for evaluating the model.

418

419 **8. Synthetic models for testing the new modeling guideline**

420   We firstly test our stepwise inversion scheme by synthetic datasets generated by thermo-

421 kinematic models modified from Braun et al. (2012) (their Fig. 9). The synthetic age dataset is

422 produced by *Pecube* using the following parameters: a steady-state topography with a 20-km

423 wavelength and a 2-km relief, a model block thickness of 30 km with a basal temperature of 600 °C,

424 a thermal diffusivity of 25 km^2/Myr, a sea level temperature of 10 °C, a lapse rate of 5 °C/km.

425 Worth noting is that these parameters are the same as Braun et al. (2012). For model details, see

426 Braun et al. (2012). For model setup see the supplementary Figure S1.

427   Synthetic AFT and AHe ages (supplementary Tables T1) were calculated for both surface

428 and borehole samples for four different exhumation histories. The synthetic models a and b are

429 characterized by a sudden decrease in exhumation rate from 1 km/Myr to 0.1 km/Myr (model-a,

430 same as the that shown in the Fig. 9 of Braun et al. 2012) and 0.3 km/Myr (model-b) at 5 Ma,

431 respectively. The models c and d include a sudden increase in exhumation rate from 0.3 km/Myr

434 (model-c) and 0.1 km/Myr (model-d) to 1 km/Myr at 5 Ma, respectively. All models start from 40

435 Ma. Except for the synthetic age data (plotted in the first row of Fig. 9), these four models generate

436 modern geothermal gradients of 26.5 °C/km, 28.6 °C/km, 35.5 °C/km and 34 °C/km for the

437 uppermost 2-km crust, respectively.

438   Inversion of rock exhumation history used a start time of 20 Ma and a time interval length

439 of 1.0 Myr for all synthetic datasets, which were assigned with a 6% uncertainty. As shown by the

440 modelling output visualized in Fig. 9a, our inversion of the rock exhumation from the synthetic

441 dataset-a finds an optimal initial geothermal gradient of 22 °C/km and *a priori* rate of 0.85 ± 0.25

442 km/Myr, and yields a decrease in exhumation rates from ~0.9 km/Myr (before 6 Ma) to 0.3-0.1

443 km/Myr (4-0 Ma), via a gradual decrease during 6-4 Ma. The data has no resolution for the

444 exhumation history before 10 Ma. Comparing to the synthetic model (abrupt decrease from 1

445 km/Myr to 0.1 km/Myr at 5 Ma), the rates before 5 Ma are underestimated by 0.1 km/Myr, whereas

446 the values after 5 Ma overestimated by 0.1-0.3 km/Myr.

447   The inversion for the synthetic dataset-b results in an optimal initial geothermal gradient

448 of 21.7 °C/km and *a priori* rate of 0.81 ± 0.24 km/Myr, and an increase in exhumation rates from

449 ~0.85 (before 5 Ma) km/Myr to 0.4-0.5 km/Myr (4-0 Ma), via a gradual decrease during 5-4 Ma

450 (Fig. 9b). Comparing to the synthetic model (abrupt decrease from 1 km/Myr to 0.3 km/Myr at 5

451 Ma), the rates before 5 Ma are underestimated, whereas the values before 5 Ma are overestimated

452 by ~0.1-0.2 km/Myr.

453   The inversion for the synthetic dataset-c yields an optimal initial geothermal gradient of

454 24.3 °C/km and *a priori* rate of 0.55 ± 0.17 km/Myr, and a decrease in exhumation rates from

455 ~0.45-0.3 km/Myr (before 5 Ma) to 1.0 km/Myr (3-0 Ma), via a gradual increase during 5-3 Ma

456 (Fig. 9c). Comparing to the synthetic model (abrupt decrease from 0.3 km/Myr to 1.0 km/Myr at

5 Ma), the rates during 5-3 Ma are underestimated, whereas the rates before 5 Ma overestimated by 0-0.15 km/Myr.

The inversion for the synthetic dataset-d produces an optimal initial geothermal gradient of 24.5 °C/km and *a priori* rate of 0.25 ± 0.08 km/Myr, and an increase in exhumation rates from ~0.1-0.2 km/Myr (before 5 Ma) to 1.0 km/Myr (3-0 Ma), via a gradual decrease during 5-3 Ma (Fig. 9d). Comparing to the synthetic model (abrupt decrease from 1 km/Myr to 0.3 km/Myr at 5 Ma), the rates before 5 Ma are slightly overestimated, whereas the values during 5-3 Ma are underestimated.

To summarize, the inverted rock exhumation histories for the four synthetic datasets match the whole picture of the synthetic "truth", but the variations in exhumation are underestimated, and the sharp changes at 5 Ma are smoothed. It is worth noting that inversions using only surface samples produce similar results (supplementary Fig. S2).

9. Natural examples for testing the new modeling guideline

Below we use three examples to demonstrate our new method. The Denali data is used again for demonstrating the efficiency of our method in finding the proper initial geothermal gradient and the *a priori* exhumation rate. Then, we further test our method using the Himalayan Dhanladar range and KTB borehole (the Continental Deep Drilling Project in Germany) thermochronologic data for representing regions of fast and slow erosion, respectively.

9.1 The Denali transect

Using the stepwise inversion modeling guideline, the Denali transect yields an exhumation history generally similar with that of the reference model (Fig. 10a). Differences in the *a priori* parameters include that the new inversion finds and uses an initial geothermal gradient of

484 25.2 °C/km (slightly higher than that of the reference model), *a priori* erosion rate of 0.46 ± 0.23

485 km/Myr (slightly lower than that of the reference model) and a time interval length of 1.5 Ma. The

486 combination of these *a priori* parameters result in a major increase in erosion rate to 0.55-0.6

487 km/Myr at 6 Ma, which is 1.5 Myr later than that of the reference model (7.5 Ma). The subtle

488 differences from the reference model mainly result from the time interval length used in these

489 models. Comparing the misfit values, the new model produces slightly better fits than the reference

490 model, with the *a posterior* misfit values of 1.81 and 0.11 for the observed age and geothermal

491 data.

492

493   9.2 Himalayan Dharladar range transect

494   AFT and ZHe data from the Dharladar range in the northwestern Himalayas, reported in

495 the publications by Deeken et al. (2011) and Thiede et al. (2017) are used as an example for regions

496 of young cooling ages and fast exhumation. The samples were collected in an elevation range

497 between 1.5 and 4.5 km, covering a topographic relief of 3 km within a spatial distance of ~15 km

498 on the hanging wall of the main central thrust of the Himalayan fold-thrust-belt (Deeken et al.,

499 2011; Thiede et al., 2017). AER slope regression of ZHe and AFT ages performed in Deeken et al.

500 (2011) produced apparent erosion rates of ~2.8 km/Myr and ~0.2 km/Myr for the time intervals

501 6.4–14.5 Ma and 1.7–3.7 Ma, respectively, implying a potential increase in erosion rates at ~3.7-

502 6.4 Ma. Using geothermal gradients of 25-45 °C/km, time-averaged erosion rates were estimated

503 as 0.8-2.0 km/Myr since 3.7 Ma (Deeken et al., 2011).

504   The modelling of the Dharladar range data uses a modern geothermal gradient constraint

505 of 45 ± 8 °C/km (Deeken et al., 2011). The relatively large uncertainty is assigned for the

506 geothermal gradient, because of the absence of direct geothermal measurements in the study area.

532   Our exhumation inversion for the AER data using the stepwise modeling guideline yields relatively

533   slow rates of 0.1-0.6 km/Myr and fast rates of 1.2-1.6 km/Myr before and after ~3 Ma, respectively

534   (Fig. 10b). The abrupt increase of exhumation rates at ~3 Ma is generally consistent with the

535   estimates from the slope regression results of Deeken et al. (2011). However, the inverted

536   exhumation rates since 3 Ma are significantly lower than the estimation from the AER slope (~2.8

537   km/Myr), which is likely due to the overestimation of exhumation of the AER slope due to

538   topographic perturbation of isotherms. Such a perturbation is a function of exhumation rates: the

539   higher the exhumation, the larger the perturbation (Glotzbach et al., 2015). The modelling yields

540   a history of the geothermal gradient that gradually increases to a modern value of ~46 °C/km, close

541   to the input value (45 ± 8 °C/km).

542

543   9.3 KTB borehole

544   The KTB borehole yields a large thermochornologic and geochronologic age data

545   (Warnock and Zeitler, 1998; Stockli and Farley, 2004). Previous studies suggest the borehole are

546   truncated by multiple faults, which offset the age-depth relationship (Wagner et al., 1997). Here

547   we use the data at depths shallower than 1 km, where data are abundant and have linear relationship

548   with depths.

549   The KTB apatite, zircon and titanite (U-Th)/He (AHe, ZHe and THe) and AFT age data

550   vary largely between 85-50 Ma. These clustered ages have been interpreted as indicating a late

551   Cretaceous phase of exhumation, followed by slow exhumation (Wagner et al., 1997; Stockli and

552   Farley, 2004), as also shown by previous thermal history reconstructions based on k-feldspar

553   ^{40}Ar/^{39}Ar data (Warnock and Zeitler, 1998).

Deleted: strategy
Deleted: 2
Deleted: 4
Deleted: relatively
Deleted: 3
Deleted: 5
Deleted: 6-5
Deleted: 9b
Deleted: 6-
Deleted: 5
Deleted: 44
Deleted: 8

566   Our modeling, using the AER data and a modern geothermal gradient of 27.5 ± 2.8 °C/km

567   (Clauser et al., 1997), shows that elevated exhumation rates (0.1-0.13 km/Myr) between 80-50 Ma,

568   followed by slower exhumation rates of ~0.04 km/Myr (Fig. 10c), are similar to previous estimates

569   (Wagner et al., 1997; Warnock and Zeitler, 1998; Stockli and Farley, 2004). Associated with

570   changes in exhumation, geothermal gradient gradually decreases from the peak values at 70-60

571   Ma to a value of ~28 °C/km at the present-day.

572

573   **10. Conclusion**

574   The *a priori* information has important effects on the inversion results using the least-

575   squares inversion method. Our study demonstrates the importance of geothermal gradient and the

576   *a priori* exhumation rate in estimating the exhumation history from the thermochronology data.

577   To take into account the geothermal data into the exhumation history inversion, we outlined a

578   stepwise inversion method that first searches for the appropriate initial geothermal gradient, which

579   is then used in the modelling searching for the *a priori* exhumation rate. Our modelling guideline

580   produces exhumation history and geothermal gradient that provide reasonable fits for both the

581   observed AER and modern geothermal data, as tested by datasets of both synthetic models and

582   natural samples. The code and data used in this work are available in GITHUB

583   (https://github.com/yuntao-github/A2E_app).

584

585   **Code availability**

586   The code used in this work are available in GITHUB (https://github.com/yuntao-github/A2E_app).

587

588   **Data availability**

---

601 The data used in this work are available in GITHUB (https://github.com/yuntao-github/A2E_app).

602

Author contribution

604 Yuntao Tian: Conceptualization, Methodology, Software, Data curation, Visualization,
605 Investigation, Writing- Original draft preparation. Lili Pan: Visualization, Writing- Reviewing and
606 Editing. Guihong Zhang and Xinbo Yao: Writing- Reviewing and Editing.

607

Competing interests

609 The contact author has declared that none of the authors has any competing interests.

610

Acknowledgments

612 This study is funded by the National Natural Science Foundation of China (42172229, 41888101
613 and 41772211). Discussions with Jie Hu and Donglan Zeng are gratefully appreciated. Comments
614 and suggestions from Gilby Jepson and Christoph Glotzbach clarified many points of this work.

615

References:
617 Anderson, J. L., Barth, A. P., Wooden, J. L., and Mazdab, F.: Thermometers and
618 Thermobarometers in Granitic Systems, Rev. Mineral. Geochem., 69, 121-142,
619 10.2138/rmg.2008.69.4, 2008.

620 Armstrong, P. A.: Thermochronometers in Sedimentary Basins, Rev. Mineral. Geochem., 58,
621 499-525, 10.2138/rmg.2005.58.19, 2005.

622 Ault, A. K., Gautheron, C., and King, G. E.: Innovations in (U–Th)/He, Fission Track, and
623 Trapped Charge Thermochronometry with Applications to Earthquakes, Weathering, Surface-
624 Mantle Connections, and the Growth and Decay of Mountains, Tectonics, 38, 3705-3739,
625 10.1029/2018TC005312, 2019.

627   Batt, G. E. and Brandon, M. T.: Lateral thinking: 2-D interpretation of thermochronology in

628   convergent orogenic settings, Tectonophysics, 349, 185-201, 2002.

629   Brandon, M. T., Roden-Tice, M. K., and Garver, J. I.: Late Cenozoic exhumation of the Cascadia

630   accretionary wedge in the Olympic Mountains, Northwest Washington State, Bull. Geol. Soc.

631   Am., 110, 985-1009, 1998.

632   Braun, J.: Quantifying the effect of recent relief changes on age-elevation relationships, Earth

633   Planet. Sci. Lett., 200, 331-343, 2002.

634   Braun, J.: Pecube: a new finite-element code to solve the 3D heat transport equation including

635   the effects of a time-varying, finite amplitude surface topography, Comput. Geosci., 29, 787-794,

636   2003.

637   Braun, J., van der Beek, P., Valla, P., Robert, X., Herman, F., Glotzbach, C., Pedersen, V., Perry,

638   C., Simon-Labric, T., and Prigent, C.: Quantifying rates of landscape evolution and tectonic

639   processes by thermochronology and numerical modeling of crustal heat transport using

640   PECUBE, Tectonophysics, 524-525, 1-28, 10.1016/j.tecto.2011.12.035, 2012.

641   Burbank, D. W., Blythe, A. E., Putkonen, J., Pratt-Sitaula, B., Gabet, E., Oskin, M., Barros, A.,

642   and Ojha, T. P.: Decoupling of erosion and precipitation in the Himalayas, Nature, 426, 652-655,

643   2003.

644   Clauser, C., Giese, P., Huenges, E., Kohl, T., Lehmann, H., Rybach, L., Šafanda, J., Wilhelm,

645   H., Windloff, K., and Zoth, G.: The thermal regime of the crystalline continental crust:

646   Implications from the KTB, J Geophy Res: Solid Earth, 102, 18417-18441,

647   https://doi.org/10.1029/96JB03443, 1997.

648   Deeken, A., Thiede, R. C., Sobel, E. R., Hourigan, J. K., and Strecker, M. R.: Exhumational

649   variability within the Himalaya of northwest India, Earth Planet. Sci. Lett., 305, 103-114,

650   10.1016/j.epsl.2011.02.045, 2011.

651   Dodson, M. H.: Closure temperature in cooling geochronological and petrological systems,

652   Contrib. Mineral. Petrol., 40, 259-274, 1973.

653   Ehlers, T. A.: Crustal Thermal Processes and the Interpretation of Thermochronometer Data,
654   Rev. Mineral. Geochem., 58, 315-350, 10.2138/rmg.2005.58.12, 2005.

655   Ehlers, T. A. and Farley, K. A.: Apatite (U-Th)/He thermochronometry: methods and
656   applications to problems in tectonic and surface processes, Earth Planet. Sci. Lett., 206, 1-14,
657   2003.

658   Fitzgerald, P. G., Sandiford, M., Barrett, P. J., and Gleadow, A. J. W.: Asymmetric extension
659   associated with uplift and subsidence in the Transantarctic Mountains and Ross Embayment,
660   Earth Planet. Sci. Lett., 81, 67-78, http://dx.doi.org/10.1016/0012-821X(86)90101-9, 1986.

661   Fitzgerald, P. G., Sorkhabi, R. B., Redfield, T. F., and Stump, E.: Uplift and denudation of the
662   central Alaska Range: A case study in the use of apatite fission track thermochronology to
663   determine absolute uplift parameters, J Geophy Res: Solid Earth, 100, 20175-20191,
664   doi:10.1029/95JB02150, 1995.

665   Fox, M., Herman, F., Kissling, E., and Willett, S. D.: Rapid exhumation in the Western Alps
666   driven by slab detachment and glacial erosion, Geology, 43, 379-382, 2015.

667   Fox, M., Herman, F., Willett, S. D., and May, D. A.: A linear inversion method to infer
668   exhumation rates in space and time from thermochronometric data, Earth Surf. Dynam., 2, 47-
669   65, 10.5194/esurf-2-47-2014, 2014.

670   Gallagher, K.: Transdimensional inverse thermal history modelling for quantitative
671   thermochronology, J. Geophys. Res., 117, B02408, doi:10.1029/2011JB008825., 2012.

672   Glotzbach, C., Braun, J., and van der Beek, P.: A Fourier approach for estimating and correcting
673   the topographic perturbation of low-temperature thermochronological data, Tectonophysics, 649,
674   115-129, https://doi.org/10.1016/j.tecto.2015.03.005, 2015.

675   Herman, F., Seward, D., Valla, P. G., Carter, A., Kohn, B., Willett, S. D., and Ehlers, T. A.:
676   Worldwide acceleration of mountain erosion under a cooling climate, Nature, 504, 423-426,
677   2013.

678 House, M. A., Wernicke, B. P., and Farley, K. A.: Paleo-geomorphology of the Sierra Nevada,
679 California, from (U-Th)/He ages in apatite, Am. J. Sci., 301, 77-102, 2001.

680 Hu, S. B., Raza, A., Min, K., Kohn, B. P., Reiners, P. W., Ketcham, R. A., Wang, J. Y., and
681 Gleadow, A. J. W.: Late Mesozoic and Cenozoic thermotectonic evolution along a transect from
682 the north China craton through the Qinling orogen into the Yangtze craton, central China,
683 Tectonics, 25, 10.1029/2006TC001985., 2006.

684 Jiao, R., Herman, F., and Seward, D.: Late Cenozoic exhumation model of New Zealand:
685 Impacts from tectonics and climate, Earth-Science Reviews, 166, 286-298,
686 https://doi.org/10.1016/j.earscirev.2017.01.003, 2017.

687 Ketcham, R. A.: Forward and Inverse Modeling of Low-Temperature Thermochronometry Data,
688 Rev. Mineral. Geochem., 58, 275-314, 10.2138/rmg.2005.58.11, 2005.

689 Laslett, G., Green, P. F., Duddy, I., and Gleadow, A.: Thermal annealing of fission tracks in
690 apatite 2. A quantitative analysis, Chem. Geol., 65, 1-13, 1987.

691 Mancktelow, N. S. and Grasemann, B.: Time-dependent effects of heat advection and
692 topography on cooling histories during erosion, Tectonophysics, 270, 167-195,
693 https://doi.org/10.1016/S0040-1951(96)00279-X, 1997.

694 McInnes, B. I. A., Evans, N. J., Fu, F. Q., and Garwin, S.: Application of Thermochronology to
695 Hydrothermal Ore Deposits, Rev. Mineral. Geochem., 58, 467-498, 10.2138/rmg.2005.58.18,
696 2005.

697 Reiners, P. W. and Brandon, M. T.: Using thermochronology to understand orogenic erosion,
698 Ann Rev Earth Planet Sci, 34, 419-466, 2006.

699 Schildgen, T. F., van der Beek, P. A., Sinclair, H. D., and Thiede, R. C.: Spatial correlation bias
700 in late-Cenozoic erosion histories derived from thermochronology, Nature, 559, 89-93,
701 10.1038/s41586-018-0260-6, 2018.

702 Stalder, N. F., Herman, F., Fellin, M. G., Coutand, I., Aguilar, G., Reiners, P. W., and Fox, M.:
703 The relationships between tectonics, climate and exhumation in the Central Andes (18–36°S):

704   Evidence from low-temperature thermochronology, Earth-Science Reviews, 210, 103276,

705   https://doi.org/10.1016/j.earscirev.2020.103276, 2020.

706   Stockli, D. F. and Farley, K. A.: Empirical constraints on the titanite (U–Th)/He partial retention

707   zone from the KTB drill hole, Chem. Geol., 207, 223-236,

708   https://doi.org/10.1016/j.chemgeo.2004.03.002, 2004.

709   Sutherland, R., Gurnis, M., Kamp, P. J. J., and House, M. A.: Regional exhumation history of

710   brittle crust during subduction initiation, Fiordland, southwest New Zealand, and implications for

711   thermochronologic sampling and analysis strategies, Geosphere, 5, 409-425,

712   10.1130/GES00225.1, 2009.

713   Tarantola, A.: Inverse Problem Theory and Methods for Model Parameter Estimation, SIAM,

714   Philadelphia2005.

715   Thiede, R., Robert, X., Stübner, K., Dey, S., and Faruhn, J.: Sustained out-of-sequence

716   shortening along a tectonically active segment of the Main Boundary thrust: The Dhauladhar

717   Range in the northwestern Himalaya, Lithosphere, 9, 715-725, 10.1130/L630.1, 2017.

718   Tian, Y., Kohn, B. P., Hu, S., and Gleadow, A. J. W.: Synchronous fluvial response to surface

719   uplift in the eastern Tibetan Plateau: Implications for crustal dynamics, Geophys. Res. Lett., 42,

720   29-35, 10.1002/2014GL062383, 2015.

721   Turcotte, D. and Schubert, G.: Geodynamics, Cambridge Univiversity Press2002.

722   Valla, P. G., van der Beek, P. A., and Braun, J.: Rethinking low-temperature thermochronology

723   data sampling strategies for quantification of denudation and relief histories: A case study in the

724   French western Alps, Earth Planet. Sci. Lett., 307, 309-322, 10.1016/j.epsl.2011.05.003, 2011.

725   van der Beek, P. and Schildgen, T. F.: Short communication: age2exhume – a MATLAB/Python

726   script to calculate steady-state vertical exhumation rates from thermochronometric ages and

727   application to the Himalaya, Geochronology, 5, 35-49, 10.5194/gchron-5-35-2023, 2023.

728   van der Beek, P. A., Valla, P. G., Herman, F., Braun, J., Persano, C., Dobson, K. J., and Labrin,

729   E.: Inversion of thermochronological age-elevation profiles to extract independent estimates of

730 denudation and relief history -- II: Application to the French Western Alps, Earth Planet. Sci.

731 Lett., 296, 9-22, DOI: 10.1016/j.epsl.2010.04.032, 2010.

732 Vermeesch, P.: IsoplotR: A free and open toolbox for geochronology, Geoscience Frontiers, 9,

733 1479-1493, https://doi.org/10.1016/j.gsf.2018.04.001, 2018.

734 Wagner, G. A., Coyle, D. A., Duyster, J., Henjes-Kunst, F., Peterek, A., Schröder, B., Stöckhert,

735 B., Wemmer, K., Zulauf, G., Ahrendt, H., Bischoff, R., Hejl, E., Jacobs, J., Menzel, D., Lal, N.,

736 Van den haute, P., Vercoutere, C., and Welzel, B.: Post-Variscan thermal and tectonic evolution

737 of the KTB site and its surroundings, J Geophy Res: Solid Earth, 102, 18221-18232,

738 https://doi.org/10.1029/96JB02565, 1997.

739 Warnock, A. C. and Zeitler, P. K.: 40Ar/39Ar thermochronometry of K-feldspar from the KTB

740 borehole, Germany, Earth Planet. Sci. Lett., 158, 67-79, https://doi.org/10.1016/S0012-

741 821X(98)00044-2, 1998.

742 Whipp Jr., D. M., Ehlers, T. A., Blythe, A. E., Huntington, K. W., Hodges, K. V., and Burbank,

743 D. W.: Plio-Quaternary exhumation history of the central Nepalese Himalaya: 2.

744 Thermokinematic and thermochronometer age prediction model, Tectonics, 26,

745 10.1029/2006tc001991, 2007.

746 Willett, S. D. and Brandon, M. T.: Some analytical methods for converting thermochronometric

747 age to erosion rate, Geochem. Geophys. Geosyst., 14, 209-222, 10.1029/2012gc004279, 2013.

748 Willett, S. D., Herman, F., Fox, M., Stalder, N., Ehlers, T. A., Jiao, R., and Yang, R.: Bias and

749 error in modelling thermochronometric data: resolving a potential increase in Plio-Pleistocene

750 erosion rate, Earth Surf. Dynam. Discuss., 2020, 1-78, 10.5194/esurf-2020-59, 2020.

751 Zeitler, P., Meltzer, A., Koons, P., Craw, D., Hallet, B., Chamberlain, C., Kidd, W., Park, S.,

752 Seeber, L., Bishop, M., and Shroder, J. F.: Erosion, Himalayan Geodynamics, and the

753 Geomorphology of Metamorphism, GSA Today, 11, 4-9, 10.1130/1052-

754 5173(2001)011<0004:EHGATG>2.0.CO;2, 2001.

755
756
757

758 **Figures captions:**
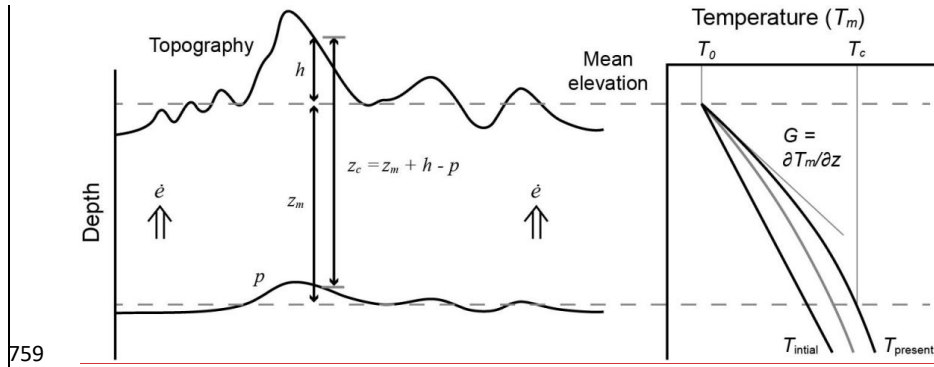
760 Figure 1. Schematics showing the relationship among closure depth (z_c), topography and its

761 perturbation (p). The parameter h denotes the difference between the sample and the mean

762 elevation, and z_m the depth of the closure temperature (T_c, the lower dashed line) derived from

763 the mean elevation (upper dashed line) and intial temperature field ($T_{initial}$) and exhumation

764 history ($\dot{e}$).

765

766

767
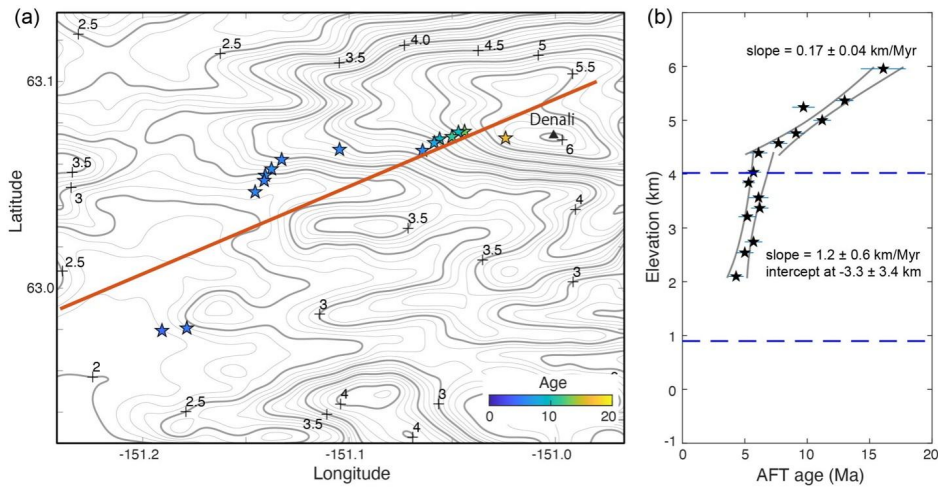
Figure 2. (a) Distribution of AFT age data (pentagons, colored by age values) over the elevation

contour map computed using the SRTM30 data of the Denali massif in Alaska. AFT data

sourced from Fitzgerald et al. (1995). (b) AER and the slope fitting results using isoplotR

(Vermeesch, 2018). AER fitting of ages older than 6.7 Ma yields a slope of 0.17 ± 0.04 km/Myr;

whereas the fitting of ages between 6.5 Ma and 4.3 Ma produces a slope of 1.2 ± 0.6 km/Myr

and an intercept at -3.3 ± 3.4 km. The upper and lower dashed lines denote the mean elevation

(4.02 km) and the depth of the nominal closure temperature (110 °C), calculated using the

modern geothermal gradient (38.9 °C/km) and the surface temperature (-12 °C).

776
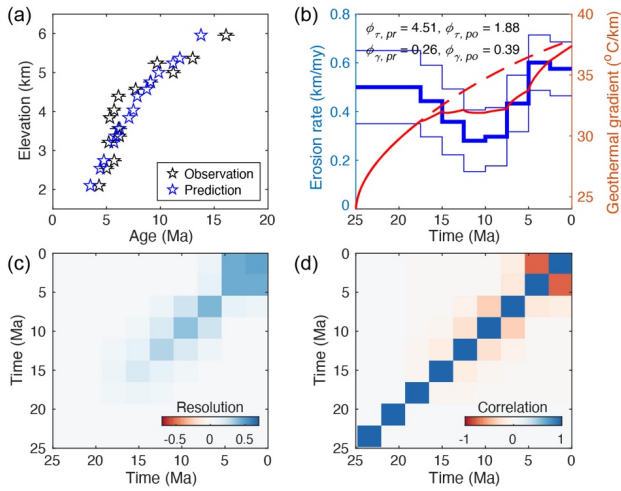
Figure 3. Inputs and outputs of the reference model for the Denali AFT. (a) Comparison between the observed (in black) and predicted (in blue) AER. (b) The *a posterior* exhumation history generated by the reference model. Thick and thin lines are the mean and one standard deviation of the inverted exhumation history. The red dash and solid lines are the history of the geothermal gradients, predicted by the *a priori* and *a posterior* models, respectively. (c) and (d) Plots of the resolution and correlation matrix.
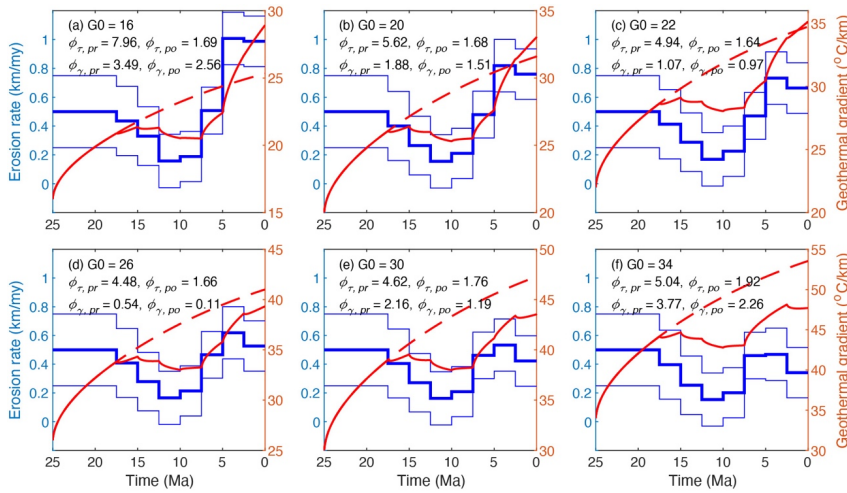
784

785 Figure 4. Histories of exhumation and geothermal gradients, predicted by models using different

786 initial geothermal gradients between 18 °C/km and 34 °C/km. The blue thick and thin lines are

787 the mean and one standard deviation of the inverted exhumation history. The red dash and solid

788 lines are the history of the geothermal gradients, predicted by the *a priori* and *a posterior*

789 models, respectively. Except for the initial geothermal gradient, other parameters are the same as

790 the reference model. Comparing to the reference model which used an initial geothermal gradient

791 of 24 °C/km (Fig. 3), models using a lower initial geothermal gradient yield relatively higher

792 exhumation rates (panels a-c), whereas those using a higher gradient produce lower exhumation

793 rates (panels d-f).

794

795
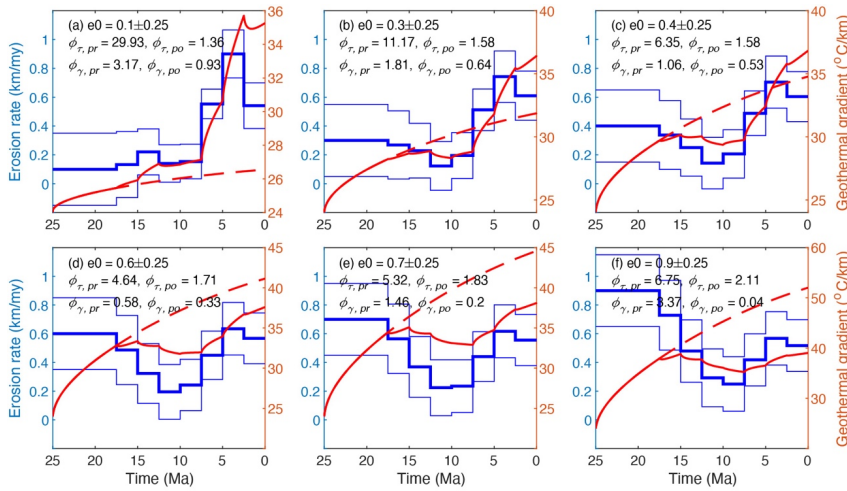
Figure 5. Histories of exhumation and geothermal gradients, predicted by models using different

a priori mean values of the exhumation rates, ranging from 0.1 km/Myr to 0.9 km/Myr. Other

parameters are the same as the reference model. For explanation of the plotted lines, see Figure

4. Comparing to the reference model which used *a priori* mean exhumation of 0.5 km/Myr (Fig.

3), models using a lower *a priori* exhumation yield relatively higher exhumation rates for the last

three stages (7.5 - 0 Ma) (panels a-c), whereas those using a higher *a priori* exhumation produce

lower exhumation rates for the last three stages (panels d-f).

803
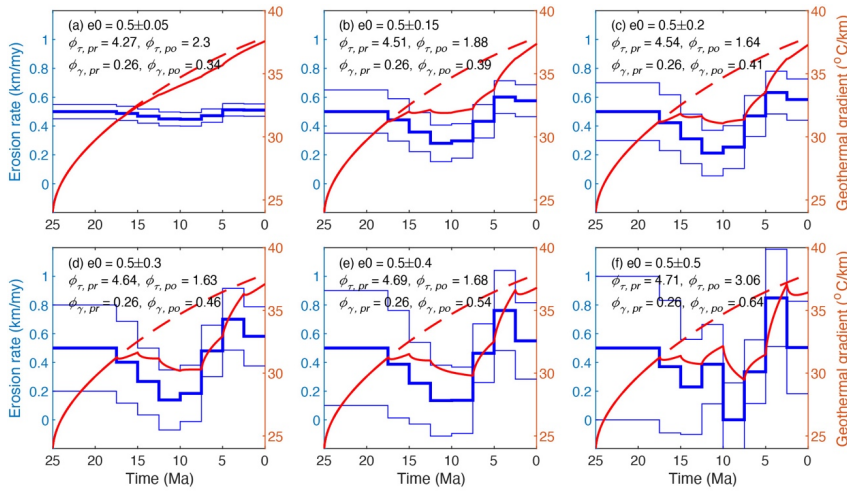
804

805 Figure 6. Histories of exhumation and geothermal gradients, predicted by models using different

806 *a priori* variance values (between 0.05 km/Myr and 0.5 km/Myr) of the exhumation rates (0.5

807 km/ Myr). Other parameters are the same as the reference model. For explanation of the plotted

808 lines, see Figure 4. Comparing to the reference model which used *a priori* variance of the

809 exhumation (0.25 km/Myr) (Fig. 3), models using a lower *a priori* variance yield limited

810 variations and uncertainties in exhumation (panels a-c), whereas those using a higher *a priori*

811 variance produce larger variations and uncertainties (panels d-f).

812
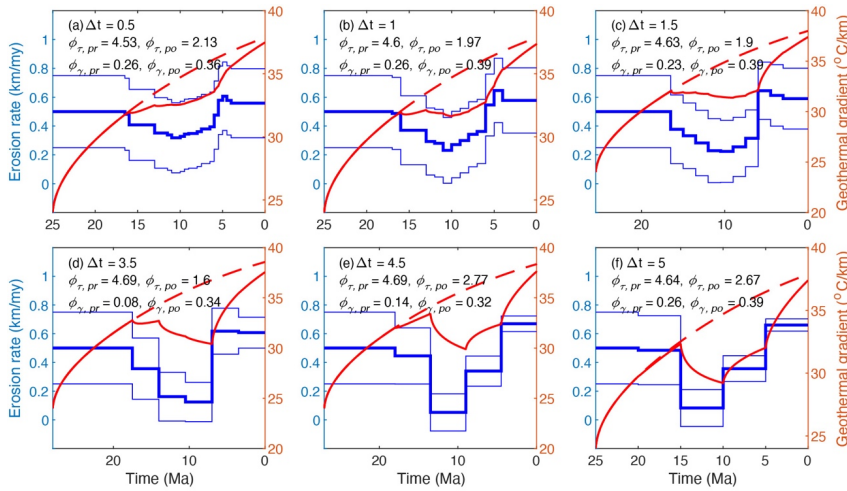
Figure 7. Histories of exhumation and geothermal gradients, predicted by models using different time interval lengths. Other parameters are the same as the reference model. For explanation of the plotted lines, see Figure 4. Comparing to the reference model which used a time interval length of 2.5 Ma (Fig. 3), models using smaller time interval lengths yield lower variations in exhumation (panels a-c) than other using larger time interval lengths (panels d-f).
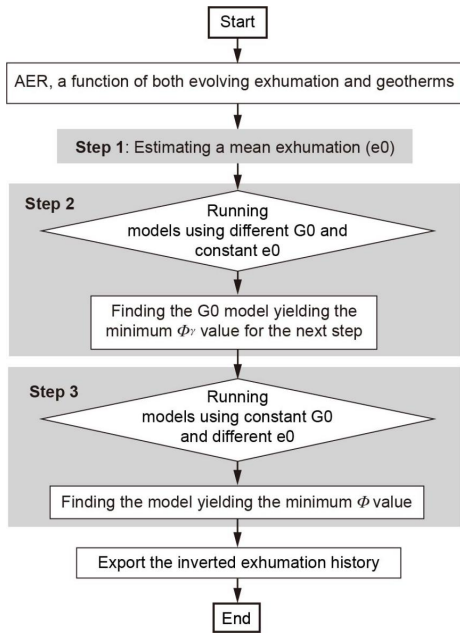
820

821 Figure 8. Flow chat of a stepwise modeling method, which includes three main steps. The first

822 step estimates a mean exhumation rate (e0) using the nominal closure temperatures, modern

823 geothermal gradient and sample ages. The mean rate is used in the second step which runs a set

824 of models using different initial geothermal gradients for optimizing the initial geothermal

825 model. The third step runs a set of models using different *a priori* exhumation rates, which is

826 generated around the mean rate, and the optimized initial geothermal model by the second step,

827 to find the best model that yields the minimum misfit to both age data and modern geothermal

828 gradient.

829

832
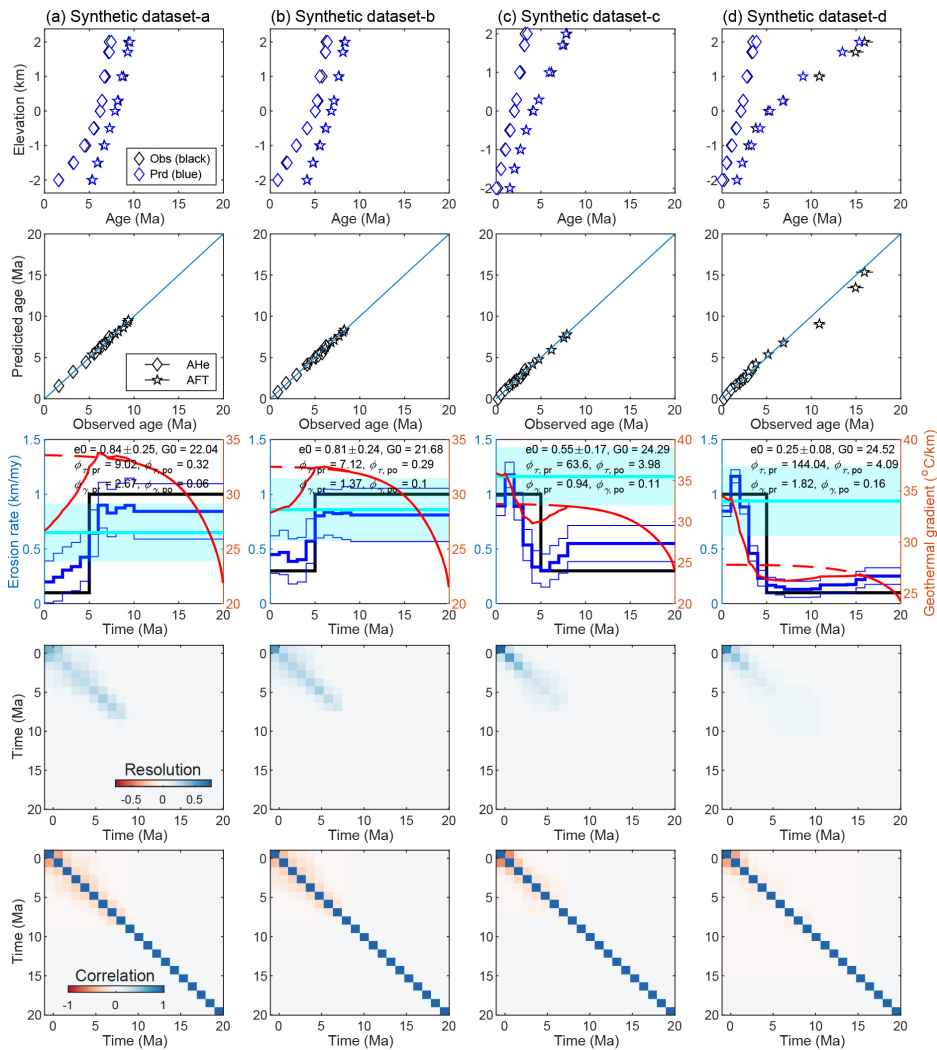
Figure 9. The best-fit model for the synthetic dataset-a, -b, -c and -d using the modeling method

shown in figure 8. First row: Comparison between the observed (in black) and predicted (in blue)

AER. Second row: plots of observed and modeled ages. Third row: Histories of exhumation and

geothermal gradients. The black line marks the "true" exhumation history used for simulating the

837 age dataset, whereas the blue thick and thin lines are the mean and one standard deviation of the

838 inverted exhumation. The red dash and solid lines are the history of the geothermal gradients,

839 predicted by the *a priori* and *a posterior* models, respectively, whereas the cyan line and polygon

840 denotes the modern geothermal gradient. Fourth and bottom row: Plots of the resolution and

841 correlation matrix.

842

843
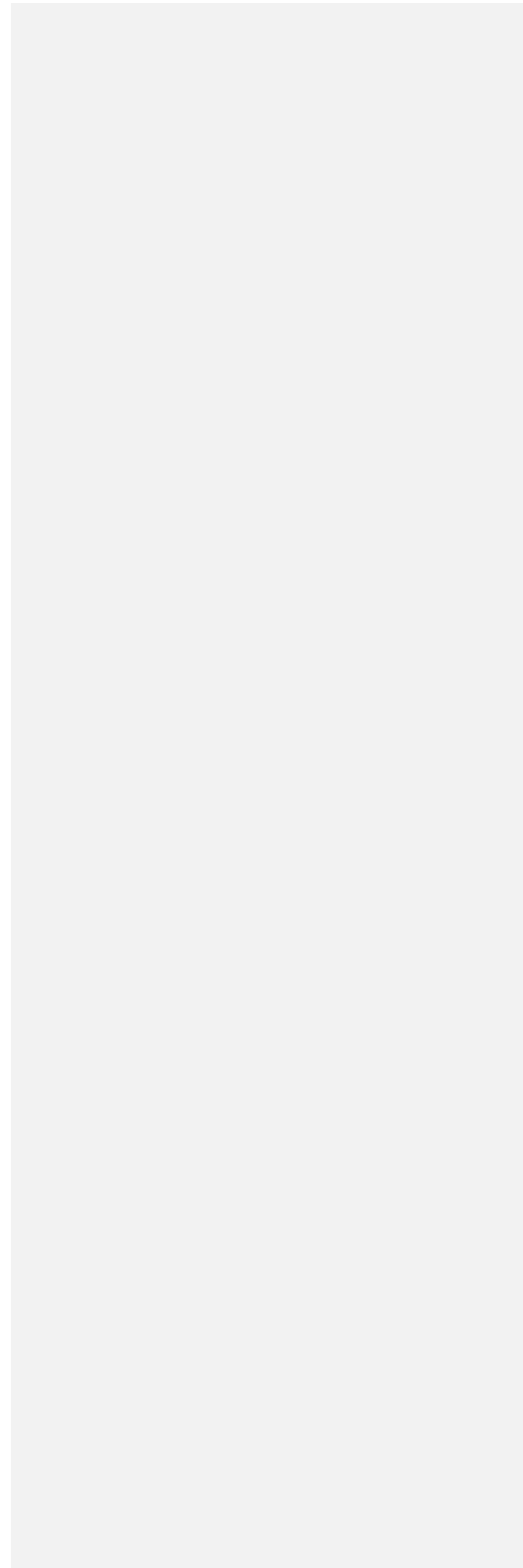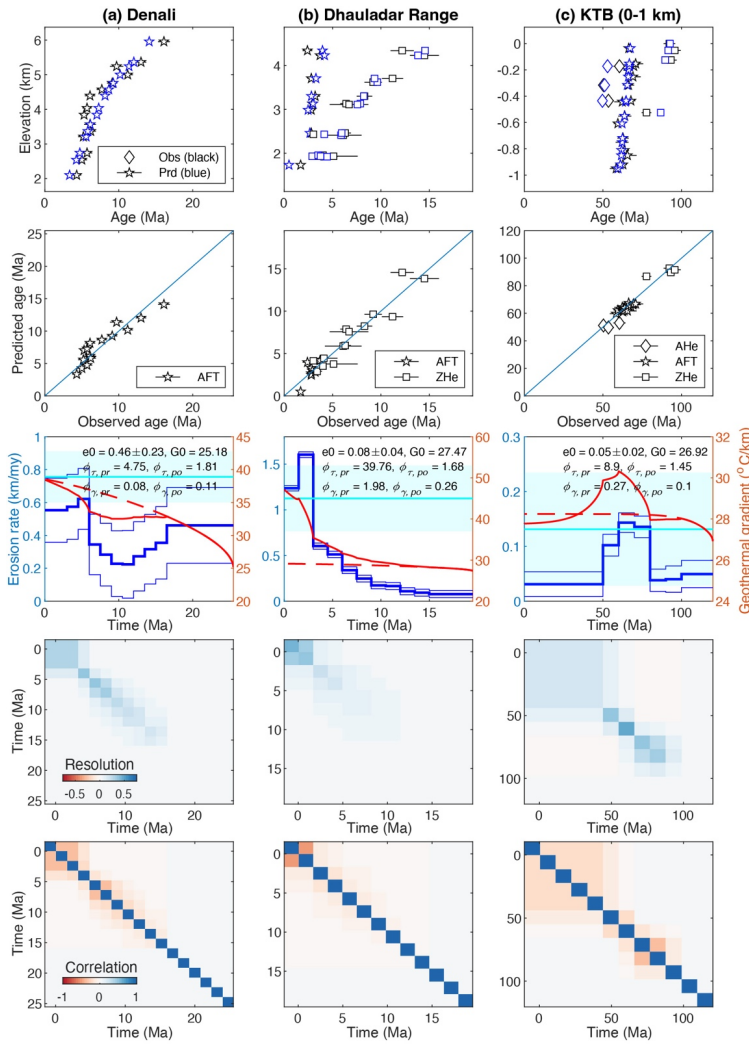
Figure 10. The best-fit model for the Denali (a), Dhanladar range (b) and upper KTB (c)

transects, using the modeling method shown in figure 8. See Fig. 8 for panel interpretations.